

On the Influence of Resonant Scattering on Cosmic Microwave Background Polarisation Anisotropies

C. Hernández-Monteagudo^{1*}, J.A. Rubiño-Martín² and R.A. Sunyaev^{3,4}

¹*Department of Physics and Astronomy, University of Pennsylvania, 209 South 33rd Str., 19104-6393 Philadelphia, USA*

²*Instituto de Astrofísica de Canarias, C/ Vía Láctea, s/n, 38200, La Laguna, Tenerife, Spain*

³*Max Planck Institut für Astrophysik (MPA), Karl-Schwarzschild Str. 1, D-85740, Garching bei München, Germany*

⁴*Space Research Institute (IKI), Profsoyuznaya 84/32, Moscow 117810, Russia*

ABSTRACT

We implement the theory of resonant scattering in the context of Cosmic Microwave Background (CMB) polarisation anisotropies. We compute the changes in the E-mode polarisation (EE) and Temperature E-mode (TE) CMB power spectra introduced by the scattering on a resonant transition with a given optical depth τ_X and polarisation coefficient E_1 . The latter parameter, accounting for how anisotropic the scattering is, depends on the exchange of angular momentum in the transition and enables, *a priori*, to distinguish among different possible resonances. We use this formalism in two different scenarios: cosmological recombination and cosmological reionisation. In the context of cosmological recombination, we compute predictions in frequency and multipole space for the change in the TE and EE power spectra introduced by scattering on the H_α and P_α lines of Hydrogen. This constitutes a fundamental test for the standard model of recombination, and the sensitivity it requires is comparable to that needed in measuring the primordial CMB B-mode polarisation component. In the context of reionisation, we study the scattering off metals and ions produced by the first stars, and find that polarisation anisotropies, apart from providing a consistency test for intensity measurements, give some insight on how reionisation evolved: since they keep memory of how anisotropic the line scattering is, they should be able to discern the OI $63.2\mu\text{m}$ transition from other possible transitions associated to OIII, NII, NIII, etc. The amplitude of these signals are, however, between 10 to 100 times below the (already challenging) level of CMB B-mode polarisation anisotropies.

Key words: cosmic microwave background – galaxies: clusters: general – diffuse radiation – intergalactic medium

1 INTRODUCTION

The cosmic microwave background (CMB) constitutes one of the most powerful tools in cosmology today. Observations of the angular power spectrum of the CMB intensity and polarisation anisotropies are providing constraints at the level of few percent on the values of the cosmological parameters describing our Universe within the standard cosmological scenario, (e.g. Spergel et al. (2006)). Moreover, because these anisotropies are intricately linked to the initial conditions in our Universe, they can also be used as a probe of inflation and fundamental physics. Microwave intensity (or temperature) anisotropies have recently been measured in the whole sky from large to medium ($\sim 0.2^\circ$) angular scales by the *Wilkinson Microwave Anisotropy*

Probe, (WMAP¹). WMAP measurements have been complemented by other ground-based high-angular resolution CMB experiments (Dickinson et al. 2004; Kuo et al. 2004; Readhead et al. 2004) with partial sky coverage.

On the other hand, the study of the CMB polarisation anisotropies is just starting: experiments like CAPMAP (Barkats et al. 2005) and CBI (Readhead et al. 2004) announced the first detection of CMB polarisation anisotropies in subdegree angular scales, whereas WMAP’s team managed to separate large-scale CMB polarisation anisotropies from the dominant contaminating signals produced in our Galaxy. Indeed, when trying to achieve better constraints on the theoretical models and to test the inflationary predictions, polarisation measurements are known to play an

* E-mail:carloshm@astro.upenn.edu

¹ WMAP’s URL site: <http://map.gsfc.nasa.gov>

important role in breaking some of the degeneracies present in the parameters (e.g. Page et al. 2006). Furthermore, a particular type of CMB polarisation anisotropies having particular symmetry properties (the so-called *B* modes of polarisation) are known to be closely related to tensorial modes in the metric perturbations (that is, *gravitational waves*) generated during the inflationary epoch. Therefore, it is easy to understand that the search for these polarisation anisotropies provides a unique test for both the cosmological model and fundamental physics, since to date no detection of gravitational waves has been reported.

For this reason, in the last few years an important effort has been put into measuring the polarisation angular power spectrum of the CMB, and consequently there is already a considerable number of projects (Clover, QUIET, CMBPol) pursuing the detection of the primordial *B*-mode of the CMB polarisation anisotropies. The predicted sensitivities of these experiments (10^{-2} to 10^{-4} (μK)²) will open the possibility to investigate additional interesting effects whose amplitudes were regarded as unreachable.

In particular, the resonant scattering on Hydrogen Balmer and Paschen lines at the epoch of recombination ($z \sim 1050$) is known to produce frequency-dependent temperature anisotropies in the sub-degree angular scales of the CMB, (Rubiño-Martín et al. 2005). These same lines are known to give rise to spectral distortions in the CMB black body spectrum (Rubiño-Martín et al. 2006; Chluba et al. 2006), at the relative level of $\sim 10^{-8}$, and in general of the order of $\sim 10^{-7}$ for higher series. Here we analyse the changes that these transitions introduce in the polarisation angular spectrum, and make definite predictions for the standard model of recombination. The amplitudes of the changes in the polarisation power spectrum are found to be comparable to the typical amplitudes of the *B* modes for values of the tensor-to-scalar ratio $r \sim 10^{-2} - 10^{-3}$. These signals should constitute a new probe for the end of recombination process, and may provide information about cosmological parameters and their evolution with time.

Another physical process that upcoming CMB experiments may be sensitive to is the resonant scattering off metals and molecules at high redshift. This idea is not new, and several authors have studied the effect of molecules (LiH, DH⁺) on the CMB radiation at high redshift, both from the theoretical (Dubrovich 1977, 1993) or the observational point of view, (de Bernardis et al. 1993). In Basu et al. (2004) (hereafter BHMS), a detailed theoretical study of the effect of resonant scattering of CMB photons off metals and ions was presented. In that work, it was shown that different observing frequencies would probe the resonant scattering at different redshifts. For this reason, the comparison of CMB maps obtained at different frequencies should provide information of the metal enrichment history of the Universe. This is essentially a consequence of the frequency dependent optical depth (τ_ν) that these resonant transitions give rise to. In their analysis, BHMS studied fine structure transitions of atoms and ions (CI, CII, NII, NIII, OI, OIII, etc), and found that the scattering process should be dominant over collisional excitation. Further, they exploited the fact that, as shown in Hernández-Monteagudo & Sunyaev (2005), the changes in the CMB temperature angular power spectrum are linear in τ_ν , and proposed a method to extract the metal induced signal in upcoming CMB data sets.

Hernández-Monteagudo et al. (2006) addressed the requirements that future CMB data must fulfill in order to be sensitive to the metal-induced signal. Among all of them, the most demanding was the cross-channel calibration, whose relative uncertainty had to be below τ_ν , i.e., better than $\sim 10^{-4}$. Point spread function reconstruction errors were found not to be very critical. The observing channels should be placed in an optimal frequency range of [100, 350] GHz, enabling an accurate subtraction of the thermal Sunyaev-Zel'dovich effect, (Sunyaev & Zel'dovich 1980).

In this paper, we study the changes that resonant scattering off metals introduce in the CMB polarisation angular power spectrum. The amplitude of these changes is found to be extremely small, still a factor 10 – 100 below the nominal sensitivity of proposed *B*-mode experiments. However, they would provide a parallel test for the enrichment history of the Universe, and help to distinguish the OI among other likely resonant species, like NII, NIII, CI, CII or even OIII.

This study should be understood in the context of proposed CMB polarisation measurements, that attempt to measure primordial *B*-modes of typical amplitudes 10^{-3} (μK)². Distinguishing signals of such small amplitudes demands stringent requirements not only on the sensitivity side, but also (and perhaps more importantly) on the systematic/foreground side: contaminants are now known to be orders of magnitude larger than the targeted *B*-modes, and their exquisite control and removal will be absolutely mandatory. The signals we are addressing in this paper have comparable amplitudes to the intrinsic *B*-modes: if the latter are finally measured, then these signals, containing a wealth of information about the recombination and reionisation histories of our Universe, may be accessible too.

The structure of the paper is as follows. In section 2 we implement the theory of resonant scattering in the context of CMB angular anisotropies. In Section 3 we apply our formalism to the polarisation changes introduced by the resonant scattering on H_α and P_α lines of Hydrogen during cosmological recombination. In Section 4 we address the resonant scattering on metals and ions during the end of the Dark Ages and the beginning of reionisation. We discuss our results and conclude in Section 5.

2 RESONANT SCATTERING AND CMB POLARISATION ANISOTROPIES

2.1 Background

We start by reviewing well known results on resonance radiation and CMB polarisation. These are combined in the next subsection in order to compute the changes in the CMB polarisation power spectrum for different types of transitions. The reader familiar with the formalism introduced here may therefore prefer to skip this subsection and continue in the next one.

An analysis of the polarisation state of resonance radiation coming out of a generic atomic system is presented in Hamilton (1947) and Chandrasekhar (1960). Their main result is that the resonant scattering is very close to Rayleigh scattering, although in the general case it gives rise to a smaller degree of polarisation. Indeed, the resonant scattering can be decomposed into a Rayleigh-like scattering term

(i.e., with its same angular dependence) and an isotropic scattering term. If I'_{\parallel} and I'_{\perp} denote the incident light intensities parallel and perpendicular to the scattering plane in a solid angle element around direction $\hat{\mathbf{n}}'$, then the scattered counterparts (I_{\parallel} and I_{\perp}) along direction $\hat{\mathbf{n}}$ are given by

$$\begin{pmatrix} I_{\parallel} \\ I_{\perp} \end{pmatrix} d\Omega(\hat{\mathbf{n}}) = \tau_X \left[E_1 \frac{3}{8\pi} \begin{pmatrix} \cos^2 \theta & 0 \\ 0 & 1 \end{pmatrix} + E_2 \frac{1}{8\pi} \begin{pmatrix} 1 & 1 \\ 1 & 1 \end{pmatrix} \right] \begin{pmatrix} I'_{\parallel} \\ I'_{\perp} \end{pmatrix} d\Omega(\hat{\mathbf{n}}'). \quad (1)$$

θ and τ_X are the scattering angle and optical depth, respectively. The coefficients E_1 and E_2 provide the relative weight of the Rayleigh-like and isotropic scatterings, and verify the condition $E_1 + E_2 = 1$, whereas the other coefficients (proportional to $1/4\pi$) ensure conservation of the scattered total intensity. The values of E_1 and E_2 depend on the initial value and change of the quantum number describing the angular momenta involved in the resonant transition, (Hamilton 1947).

We next write the radiative transfer equation for this scattering in terms of the Stokes parameters I ($\equiv I_{\parallel} + I_{\perp}$) and Q ($\equiv I_{\parallel} - I_{\perp}$). This scattering produces no circular polarisation, so the Stokes parameter V will be ignored. We study the radiation coming from an arbitrary point $\hat{\mathbf{n}}$ on the celestial sphere. Our axes used to define the parallel (\parallel) and perpendicular (\perp) directions are determined by the meridian and azymuthal directions at $\hat{\mathbf{n}}$, respectively. As shown in Chandrasekhar (1960), in order to compute the parameters $I(\hat{\mathbf{n}})$ and $Q(\hat{\mathbf{n}})$ in this reference frame, it is necessary to integrate in all possible directions $\hat{\mathbf{n}}'$ of incoming radiation. In this step, one must account for the different reference frames being involved. Since our scattering matrices (eq.(1)) are defined with respect to the plane of scattering, it is necessary to make two transformations of the intensities: the first one projects intensities at $\hat{\mathbf{n}}'$ into the axes parallel and normal to the scattering plane, whereas the second transforms the scattered intensities into our reference frame at $\hat{\mathbf{n}}$. Under an infinitesimally small optical depth due to the resonant transition ($\Delta\tau_X$), the radiative transfer equation yields the following changes in the I and Q parameters for the resonant scattering:

$$\Delta \begin{pmatrix} I \\ Q \end{pmatrix}(\hat{\mathbf{n}}) = \Delta\tau_X \left[- \begin{pmatrix} I \\ Q \end{pmatrix}(\hat{\mathbf{n}}) + \begin{pmatrix} I_0 - E_1 P_2(\mu) \frac{1}{2} (I_2 + Q_2 + Q_0) \\ E_1 (1 - P_2(\mu)) \frac{1}{2} (I_2 + Q_2 + Q_0) \end{pmatrix} \right]. \quad (2)$$

In this equation, the parameters I and Q have been expanded on a Legendre polynomial basis ($X(\hat{\mathbf{n}}) = \sum_l (-i)^l (2l+1) P_l(\mu) X_l$, with $X = I, Q$), $\mu \equiv \cos \theta$ and θ is the polar angle at $\hat{\mathbf{n}}$. Both I and Q are assumed to be azymuthally symmetric. This expression meets the standard Rayleigh scattering limit if $E_1 \rightarrow 1$, and shows how the intensity quadrupole alone (I_2) acts as a source for linear polarisation. At the same time, it is clear that different resonant transitions with different E_1 coefficients give rise to different levels of polarisation. We shall show below that this fact may have its relevance, since polarisation measurements may distinguish among different candidate resonant species otherwise undistinguishable with intensity measurements only: the polarisation

term $\Pi \equiv (I_2 + Q_2 + Q_0)$ is typically a few percent of I_0 , and this fact largely hides the value of E_1 from intensity observations.

In a cosmological context, we follow Ma & Bertschinger (1995) to describe the evolution of the perturbations of the photon field. They work in Fourier space, and therefore the photon distribution function $f_{\gamma}(\mathbf{k}, \mathbf{q}, \eta)$ is *a priori* dependent on comoving wavemodes \mathbf{k} , photon momenta \mathbf{q} and conformal time η . However, in cosmological perturbation theory, due to a symmetry present in the evolution equations, it is customary to work with the simplifying assumption that f_{γ} depends on the direction of the photon momentum $\mathbf{q}/q = \hat{\mathbf{n}}$ via the dot product $\hat{\mathbf{n}} \cdot \hat{\mathbf{k}} = \hat{\mathbf{n}} \cdot \mathbf{k}/k$ only, (k being the modulus of \mathbf{k} and q the modulus of \mathbf{q}). This permits to expand the photon distribution function for the polarisation state i as

$$f_{\gamma}^i(\mathbf{k}, \mathbf{q}, \eta) = f_0^i(q, \eta) \left[1 + \Psi^i(\mathbf{k}, q, \hat{\mathbf{k}} \cdot \hat{\mathbf{n}}, \eta) \right] = f_0^i(q, \eta) \left[1 + \sum_l (-i)^l (2l+1) P_l(\hat{\mathbf{k}} \cdot \hat{\mathbf{n}}) \Psi_l^i(\mathbf{k}, q, \eta) \right], \quad (3)$$

with $f_0^i(q, \eta) = 1/h^3(\exp(qc/k_B T_{CMB}[\eta]) - 1)$ the unperturbed Planck distribution function for the polarisation state i . Ψ_l^i is the vk , q and η dependent perturbation of the distribution function for the same polarisation state i . This expansion can be applied to the momentum-averaged energy distribution function for both polarisation states,

$$F_{\gamma,l}(\mathbf{k}, \eta) = \frac{\sum_{i=1}^2 \int dqq^2 f_0^i(q, \eta) q \Psi_l^i}{\sum_{i=1}^2 \int dqq^2 f_0^i(q, \eta) q}, \quad (4)$$

and for the difference of the two polarisation components,

$$G_{\gamma,l}(\mathbf{k}, \eta) = \frac{\int dqq^2 q (f_0^1(q, \eta) \Psi_l^1 - f_0^2(q, \eta) \Psi_l^2)}{\sum_{i=1}^2 \int dqq^2 f_0^i(q, \eta) q}. \quad (5)$$

These two l -dependent quantities correspond to the X_l terms in the expansion $X(\mathbf{k}, \mathbf{q}, \eta) = \sum_l (-i)^l (2l+1) P_l(\hat{\mathbf{k}} \cdot \hat{\mathbf{n}}) X_l(\mathbf{k}, q, \eta)$, with $X = F_{\gamma}, G_{\gamma}$. If now a reference system for \mathbf{q} is chosen so that the $\hat{\mathbf{z}}$ axis is parallel to $\hat{\mathbf{k}}$, then it is clear that the linear polarisation will be in the direction of changing θ , i.e., parallel to $\partial/\partial\theta$, due to the azymuthal symmetry of $f_{\gamma}(\mathbf{k}, q, \hat{\mathbf{k}} \cdot \hat{\mathbf{n}}, \eta)$ for fixed \mathbf{k} and η . Therefore, in the orthonormal basis $\{\partial/\partial\theta, \partial/\partial\phi\}$ the momentum-integrated quantity G_{γ} corresponds to the Q Stokes parameter, whereas U vanishes. Zaldarriaga & Harari (1995) formally integrated the evolution equations for $\Delta_T \equiv F_{\gamma}/4$ and $\Delta_P \equiv G_{\gamma}/4$ for every Fourier mode \mathbf{k} , (note that we have switched into temperature units). However, since the Q and U Stokes parameters are dependent on the orientation of the reference frame where they are defined, when integrating in all Fourier modes to obtain Δ_T, Δ_P along a given line of sight $\hat{\mathbf{n}}$ the following problem arises: for every new \mathbf{k} a new (rotated) reference system must be adopted, and Q and U must be transformed accordingly. Zaldarriaga & Seljak (1997) solved this problem by introducing the combinations $Q(\hat{\mathbf{n}}) \pm iU(\hat{\mathbf{n}})$ that can be easily transformed into *rotationally invariant* quantities $E(\hat{\mathbf{n}})$ and $B(\hat{\mathbf{n}})$. After projecting the three quantities $\Delta_T(\hat{\mathbf{n}})$, $E(\hat{\mathbf{n}})$ and $B(\hat{\mathbf{n}})$ on a spherical harmonic basis,

$$\Delta_{T,E,B} = \sum_{l,m} a_{l,m}^{T,E,B} Y_{l,m}(\hat{\mathbf{n}}), \quad (6)$$

they found analytical expressions for the angular power spectra $C_l^{T,E,B} = \langle a_{l,m}^{T,E,B} (a_{l,m}^{T,E,B})^* \rangle$:

$$C_l^{T,E} = (4\pi)^2 \int dk k^2 P_\phi(k) |\Delta_l^{T,E}(k, \eta_0)|^2. \quad (7)$$

$P_\phi(k)$ is the initial power spectrum of scalar perturbations, which are found not to give rise to any B mode, ($C_l^B = 0$). The transfer functions

$$\Delta_l^{T,E}(k, \eta_0) = \int_0^{\eta_0} d\eta S_{T,E}(k, \eta) f_l^{T,E} j_l(k[\eta_0 - \eta]) \quad (8)$$

are characterised by the source functions

$$S_T(k, \eta) = e^{-\tau} (\dot{\xi} + \ddot{\alpha}) + \Lambda \left(\Delta_{T,0} + \ddot{\alpha} \right) + \Lambda \left(\ddot{\alpha} + \frac{v_b}{k} \right) + \dot{\Lambda} \frac{v_b}{k} + \Lambda \left(\frac{\Pi}{4} + \frac{3\ddot{\Pi}}{4k^2} \right) + \dot{\Lambda} \frac{3\dot{\Pi}}{4k^2} + \ddot{\Lambda} \frac{3\Pi}{4k^2} \quad (9)$$

for the temperature and

$$S_E(k, \eta) = \frac{3\Lambda\Pi}{4(k[\eta_0 - \eta])^2} \quad (10)$$

for the E-mode polarisation field. $f_l^T = 1 \forall l$ and $f_l^E = \sqrt{(l+2)!(l-2)!}$. In these equations, $j_l(x)$ are spherical Bessel functions of order l , η_0 is the conformal time at the present epoch, and $\alpha \equiv (\dot{\xi} + 6\dot{\eta})/2k^2$ is a function of the metric scalar perturbations h and ξ in the synchronous gauge, used throughout this paper. The polarisation term Π , as already defined above, is the sum of the temperature quadrupole and Q monopole and quadrupole, i.e. $\Pi \equiv \Delta_{T,2} + \Delta_{P,2} + \Delta_{P,0}$, and $\Lambda = \dot{\tau}e^{-\tau}$ is the visibility function. $\dot{\tau}$ is the opacity, which, in case of Thomson scattering, reads

$$\dot{\tau}_T = a\sigma_T n_e, \quad (11)$$

with a the scale factor, σ_T the Thomson cross section and n_e the comoving free electron number density. The optical depth is defined as

$$\tau_T(\eta) = \int_\eta^{\eta_0} \dot{\tau}_T(\eta') d\eta'. \quad (12)$$

For these quantities, the subscript T denotes "Thomson scattering". Throughout this paper, dots denote derivatives with respect to conformal time η .

2.2 The Modified Visibility Function

We combine the previous results in order to compute the effect of resonant scattering on CMB anisotropies. In equation (2) we have seen that a resonant transition of optical depth $\Delta\tau_X$ erases both I and Q parameters by an amount $\Delta\tau_{rs}$, and generates new intensity by an amount proportional to $\Delta\tau_X$ as well. However, the new polarisation generated in the resonant scattering is not proportional to $\Delta\tau_X$, but to $E_1 \Delta\tau_X$. This fact requires the following modifications of eqs.(9,10) by means of the new visibility function $\tilde{\Lambda}$:

$$S_T(k, \eta) = e^{-\tau} (\dot{\xi} + \ddot{\alpha}) + \Lambda \left(\Delta_{T,0} + \ddot{\alpha} \right) + \Lambda \left(\ddot{\alpha} + \frac{v_b}{k} \right) + \dot{\Lambda} \frac{v_b}{k} + \tilde{\Lambda} \left(\frac{\Pi}{4} + \frac{3\ddot{\Pi}}{4k^2} \right) + \dot{\tilde{\Lambda}} \frac{3\dot{\Pi}}{4k^2} + \ddot{\tilde{\Lambda}} \frac{3\Pi}{4k^2}; \quad (13)$$

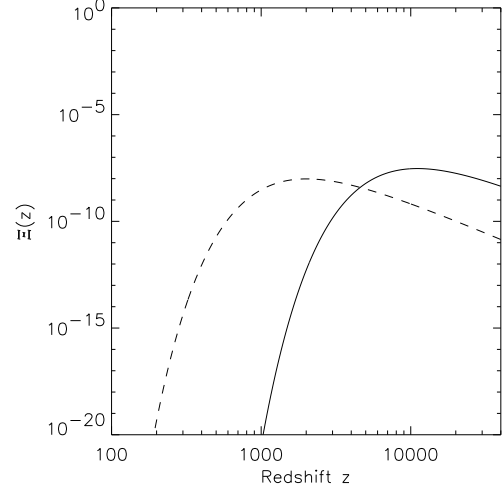


Figure 1. Function Ξ displaying the ratio of the drag force exerted by resonant scattering over the Thomson drag, for two different resonant transitions: Ly- α (solid line), and LiI 2S \rightarrow 2P [6708 Å] (dashed line). At all redshifts, Ξ is much smaller than one, making the drag force induced by resonant species negligible if compared to the Thomson drag.

$$S_E(k, \eta) = \frac{3\tilde{\Lambda}\Pi}{4(k[\eta_0 - \eta])^2}. \quad (14)$$

In this case, the total opacity and optical depth read

$$\dot{\tau}(\eta) = \dot{\tau}_T(\eta) + \dot{\tau}_X(\eta), \quad (15)$$

$$\tau(\eta) = \int_\eta^{\eta_0} (\dot{\tau}_T + \dot{\tau}_X) d\eta'. \quad (16)$$

The visibility function Λ remains unchanged in terms of τ and $\dot{\tau}$, while the new visibility function $\tilde{\Lambda}$ is defined as

$$\tilde{\Lambda} \equiv (\dot{\tau}_T + E_1 \dot{\tau}_X) e^{-\tau}. \quad (17)$$

Note that this new visibility function is coupled to the polarisation terms exclusively. The generation of anisotropies is ruled by the opacity term, which does contain E_1 , whereas the blurring of existing anisotropies is caused by the exponential of τ , which does *not* depend on E_1 . Hence, we expect that different resonant transitions with different E_1 coefficients should be discernible in those angular scales (l ranges) where the generation of new polarisation anisotropies dominates or is comparable to the blurring of old anisotropies. I.e., we shall recover no information on E_1 in the high l limit for which $\delta C_l^{TT,EE} \simeq -2\tau C_l^{TT,EE}$.

2.3 The Drag Force

The Thomson scattering influences the evolution of baryons, since they exchange momentum with the CMB photons. This interaction is accounted for by adding a momentum conservation term to the equation for the evolution of the baryon peculiar velocity, (e.g., Ma & Bertschinger (1995)):

$$\dot{v}_b = -\frac{\dot{a}}{a} v_b - i c_s^2 k \delta_b + \frac{4\bar{\rho}_\gamma}{3\bar{\rho}_b} a n_e \sigma_T \left(-\frac{3i}{4} F_{\gamma,1} - v_b \right). \quad (18)$$

v_b denotes baryon peculiar velocity, c_s is the sound speed in the baryon photon fluid before recombination, δ_b is the

comoving baryon density contrast, and $\bar{\rho}_{\gamma(b)}$ are the photon (baryon) background energy densities. Finally, $F_{\gamma,1}$ is the $l=1$ moment in the expansion of the momentum averaged photon energy distribution function, (see eq.(4)). When considering the resonant scattering, a similar term should be included in this equation. There is, however, a critical difference: Thomson scattering is frequency independent, and couples *all* photons with baryons, as opposed to resonant scattering, that couples only those photons within the thermal width of the line. Loeb (2001) uses arguments based upon the characteristic time of the drag force to conclude that it does not play any role in the case of Lithium scattering. Here we explicitly compute the drag force, for both Thomson scattering and resonant scattering, and confirm that indeed the latter can be ignored in practically all cases.

For Thomson scattering, the drag force (defined here as rate of momentum exchange per unit time and unit volume) reads

$$F_{\gamma}^T(\mathbf{k}, \eta) = (-4\pi i) \int dq q^2 \sum_{i=1}^2 f_0^i(q, \eta) q \Psi_1^i(\mathbf{k}, q, \eta) \times c \sigma_T n_e(\eta) \quad (19)$$

but for resonant scattering on a transition X , the drag force must account for limited range of frequencies that do interact with the baryons. This is introduced via by imposing a resonance condition in the momentum integration of the atom distribution function:

$$F_{\gamma}^X(\mathbf{k}, \eta) = (-4\pi i) \int dq q^2 \sum_{i=1}^2 f_0^i(q, \eta) q \Psi_1^i(\mathbf{k}, q, \eta) \times c \sigma_X \int_{\Sigma} d\mathbf{p} f_X(\mathbf{p}, \eta). \quad (20)$$

The symbol Σ denotes the subset of all possible atom momenta \mathbf{p} verifying the resonance condition. $f_X(\mathbf{p}, \eta)$ is the distribution function of the atom responsible for the transition X . For simplicity, we shall assume that all baryons are in thermal equilibrium with the CMB radiation field at all redshifts, so that the CMB temperature will characterise their Maxwell-Boltzmann distribution function. The resonance condition

$$\frac{qc}{\hbar} \left(\frac{\mathbf{p} \cdot \hat{\mathbf{n}}}{m_X c} - 1 \right) = \nu_X \quad (21)$$

can be rewritten, after accounting for the natural width of the line, as

$$\mathbf{p} \cdot \hat{\mathbf{n}} \in \left[\min \left(m_X c \left(1 - \frac{\nu_X}{\nu} \pm \frac{A_X}{4\pi} \right) \right), \max \left(m_X c \left(1 - \frac{\nu_X}{\nu} \pm \frac{A_X}{4\pi} \right) \right) \right], \quad (22)$$

A_X is the Einstein coefficient for spontaneous emission of transition X , and the ratio $A_X/2\pi$ is its natural width. m_X and ν_X denote the mass of the resonant atomic species and the resonant frequency, respectively. μ is the cosine of the angle between \mathbf{p} and $\hat{\mathbf{n}}$, ($\mu = \mathbf{p}/p \cdot \hat{\mathbf{n}}$). Since we are considering all photon frequencies, all atoms within the thermal width are counted and all of them contribute to the drag force, so the integral on the atom distribution function

yields $n_X(\eta)$, the atom number density, (see Appendix A for details). Therefore:

$$F_{\gamma}^X \simeq (-4\pi i) (c \sigma_X n_X) \frac{h A_X}{2\pi c} q_X^2 (f_0 \Psi_1)_{q_X} q_X. \quad (23)$$

I.e., momentum of amplitude $q_X \equiv h\nu_X/c$ is transferred to the atom fluid at a rate per unit volume $c \sigma_X n_X$ in a momentum-space shell of radius q_X and thickness $h\nu_X/(2\pi c)$. The photon distribution momentum $f_0 \Psi_1$ corresponds to the sum over the two polarisation states, $f_0 \Psi_1 \equiv \sum_{i=1}^2 f_0^i \Psi_1^i$. The ratio of the Thomson induced drag force and the one generated by resonant scattering reads

$$\frac{F_{\gamma}^X}{F_{\gamma}^T} \simeq \frac{\sigma_X n_X}{\sigma_T n_e} \times \left[\frac{h A_X}{2\pi c} q_X^2 (f_0(q_X, \eta) \Psi_1(\mathbf{k}, q_X, \eta)) q_X \right] \left/ \left[\int dq q^2 f_0(q, \eta) \Psi_1(\mathbf{k}, q, \eta) q \right] \right. \quad (24)$$

If we now consider that, at least *ab initio*, the $l=1$ momentum of the photon distribution function $f_0(q, \eta) \Psi_1(\mathbf{q}, q, \eta)$ is caused by gravitational sources, so that $\partial \Psi_1 / \partial q \simeq 0$, then Ψ_1 is cancelled in eq.(24), yielding

$$\frac{F_{\gamma}^X}{F_{\gamma}^T} \simeq \frac{\sigma_X n_X}{\sigma_T n_e} \left[\frac{h A_X}{2\pi c} q_X^2 f_0(q_X, \eta) q_X \right] \frac{4\pi c}{\bar{\rho}_{\gamma}} \equiv \frac{\sigma_X n_X}{\sigma_T n_e} \Xi[\eta, \nu_X]. \quad (25)$$

The ratio Ξ versus redshift is shown in Figure (1) for two resonant transitions: Ly- α (solid line) and LiI 2S \rightarrow 2P [6708 Å] (dashed line). There are two factors that make the drag force exerted by resonant transitions negligible when compared to Thomson drag: *i*) Only photons within the line width exchange momenta with the atoms, and *ii*) the line is, for most redshifts, far from the peak of the planckian photon distribution function. Therefore, for the moderate to small values of τ_X that we will be handling in this paper, the drag force can be completely ignored in our calculations.

2.4 Moderate and Low τ_X Examples

In this subsection we compute the changes in the intensity and polarisation CMB angular power spectra introduced by a resonant transition in two different limits: moderate optical depth ($\tau_X = 2$), and small optical depth ($\tau_X = 5 \times 10^{-4}$). As shown in BHMS, in the limit of low τ_X there are two competing terms: a generation term, present at scales larger than the projected horizon at the epoch of scattering, and a blurring term, accounting for the slight decrease in the amount of *previous-to-the-scattering* temperature anisotropies. The latter is dominant at small angular scales, and verifies $\delta C_l^{TT} \simeq -2\tau_X C_l^{TT}$. The former term is caused by the growth of peculiar velocities with cosmic time, and is responsible for positive δC_l 's below a multipole $l_X \sim (\eta_0 - \eta_X)/\eta_0$, (Hernández-Monteagudo & Sunyaev 2005). In the limit of high τ_X , however, the generation of new anisotropies dominate in the entire angular range, (Zaldarriaga & Loeb 2002).

We consider a resonant transition at an effective scattering redshift close to $z_X \simeq 500$, or conformal distance $\eta_X \simeq 450$ Mpc. This is close to the epoch at which Loeb

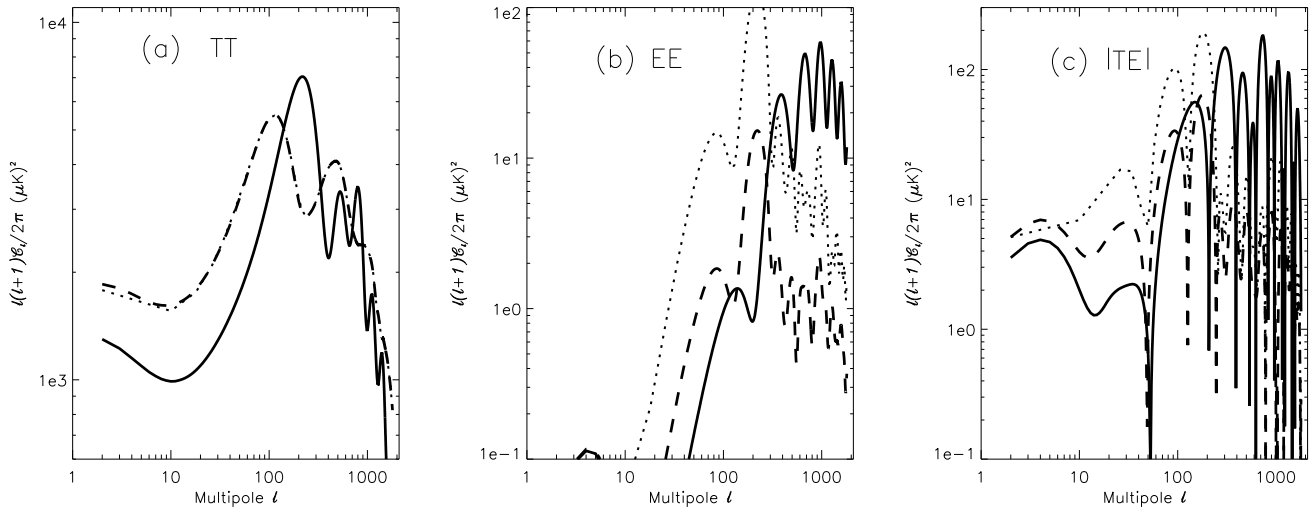


Figure 2. TT, EE and TE angular power spectra for three different scenarios: standard Λ CDM cosmology (thick solid line), standard Λ CDM cosmology plus a resonant transition placed at $z_X \simeq 500$ and $(\tau_X, E_1) = (2, 1/3)$ (dashed line), and standard Λ CDM cosmology plus a resonant transition placed at $z_X \simeq 500$ and $(\tau_X, E_1) = (2, 1)$ (dotted line).

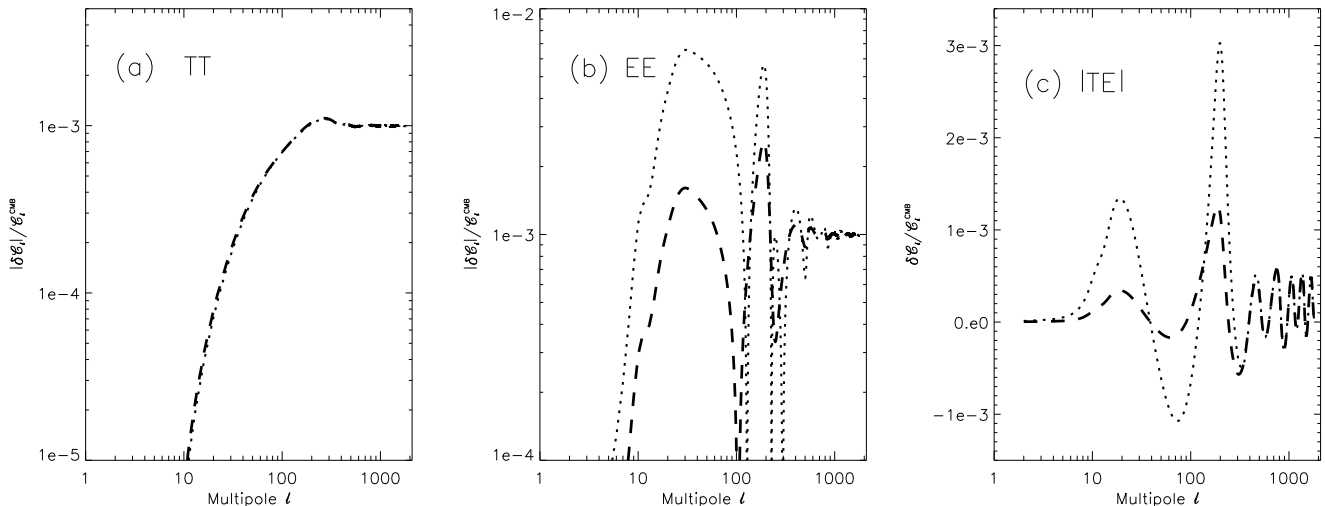


Figure 3. Relative increment of TT, EE and TE angular power spectra with respect to the standard Λ CDM scenario due to the presence of a resonant line placed at $z_X \simeq 500$ with $(\tau_X, E_1) = (5 \times 10^{-4}, 1/3)$ (dashed line) and $(\tau_X, E_1) = (5 \times 10^{-4}, 1)$ (dotted line). Note that for panels (a) and (b) we are plotting absolute values. Since the blurring of original anisotropies is independent of E_1 , both lines converge to $2\tau_X$ in the high- l range for the EE plot as well. Note that due to the change of sign of C_l^{TE} , in panel (c) we prefer to normalise by $\sqrt{C_l^{TT}C_l^{EE}}$.

(2001); Zaldarriaga & Loeb (2002) placed the resonant scattering between the CMB and the neutral Lithium via the LiI 2S \rightarrow 2P [6708 Å] resonance. Although it has been shown that at such redshifts Lithium should be ionised by Ly- α photons generated during recombination (Switzer & Hirata 2005), we choose a similar scattering redshift for comparison purposes. We use a modified version of CMBFAST (Seljak & Zaldarriaga 1996) where a new visibility function (modified as outlined in subsection (2.2)) has been introduced. Motivated by our results above, we also disconnect the drag force exerted by the atoms. We choose a gaussian profile for the line opacity,

$$\dot{\tau}_X(\eta) = \tau_X \frac{\exp - \frac{(\eta - \eta_X)^2}{2\sigma_X^2}}{\sqrt{2\pi\sigma_X^2}}. \quad (26)$$

The width of the line is taken to be one percent of η_X , but it would ultimately depend on the spectral resolution of the detector. Figure (2) shows the temperature (TT), E-mode polarisation (EE) and cross (TE) power spectra for three scenarios: the concordance Λ CDM model (thick solid lines), used as a reference model, and this reference model as seen after introducing a species giving rise to a resonant scattering of parameters $[\tau_X, E_1] = [2, 1/3]$ (dashed lines) and $[\tau_X, E_1] = [2, 1]$, (dotted lines). Panel (a) shows that different

Table 1. Possible H_α ($n = 2 \rightarrow n = 3$) and P_α ($n = 3 \rightarrow n = 4$) transitions ^(a)

Wavelength (Å)	A_{ji} (s^{-1})	i (L_J)	j (L_J)	E_1
6562.7096	5.388e+07	$P_{1/2}$	$D_{3/2}$	0.5
6562.7247	2.245e+07	$S_{1/2}$	$P_{3/2}$	0.5
6562.7517	2.104e+06	$P_{1/2}$	$S_{1/2}$	0
6562.7714	2.245e+07	$S_{1/2}$	$P_{1/2}$	0
6562.8516	6.465e+07	$P_{3/2}$	$D_{5/2}$	0.28
6562.8672	1.078e+07	$P_{3/2}$	$D_{3/2}$	0.32
6562.9093	4.209e+06	$P_{3/2}$	$S_{1/2}$	0
18750.684	5.864e+06	$P_{1/2}$	$D_{3/2}$	0.50
18750.720	3.065e+06	$S_{1/2}$	$P_{3/2}$	0.50
18750.829	6.117e+05	$P_{1/2}$	$S_{1/2}$	0
18750.881	3.065e+06	$S_{1/2}$	$P_{1/2}$	0
18751.011	7.037e+06	$P_{3/2}$	$D_{5/2}$	0.28
18751.011	1.287e+07	$D_{3/2}$	$F_{5/2}$	0.28
18751.064	3.475e+04	$D_{3/2}$	$P_{3/2}$	0.32
18751.065	1.173e+06	$P_{3/2}$	$D_{3/2}$	0.32
18751.111	1.379e+07	$D_{5/2}$	$F_{7/2}$	0.21
18751.138	9.193e+05	$D_{5/2}$	$F_{5/2}$	0.37
18751.191	3.128e+05	$D_{5/2}$	$P_{3/2}$	0.02
18751.210	1.223e+06	$P_{3/2}$	$S_{1/2}$	0
18751.225	3.475e+05	$D_{3/2}$	$P_{1/2}$	0

(a) Taken from NIST URL site:
http://physics.nist.gov/PhysRefData/ASD/lines_form.html.

values of E_1 are not discernible in the TT power spectrum, since the contribution of the polarisation terms is of the order of a few percent: in the plot these differences are visible to the eye at $l < 20$, but these are the scales more affected by Cosmic Variance. Nevertheless, the EE power spectrum shown in panel (b) provides very different estimates for different values of E_1 , making both scenarios easily discernible for this large value of τ_X . Since new anisotropies are generated in an older universe subtending a larger angle in the sky, the angular pattern of the power spectra shifts to lower multipoles, both in the TT and the EE cases. The polarisation source term $S_E(k, \eta)$ is larger at $z \sim 500$ than at decoupling (see eq.(14)), and this makes the EE power spectrum of the $[\tau_X, E_1] = [2, 1]$ of higher amplitude (dotted line above solid lines). Note that the cross-power spectra also show significant differences for the two E_1 values considered, (Fig.(2c)).

The low τ_X case, displayed in Fig.(3), also provides significant differences between the $E_1 = 1$ and the $E_1 = 1/3$ models in the TE and EE power spectra. These differences vanish in the high l limit, where the blurring term takes over and $\delta C_l \rightarrow -2\tau_X C_l$ for all values of E_1 . In case of resonant scattering on metals produced at late epochs (end of the Dark Ages and reionisation), the generation of new anisotropies arise at very large angular scales, and hence distinguishing different values of E_1 will require large sky coverage.

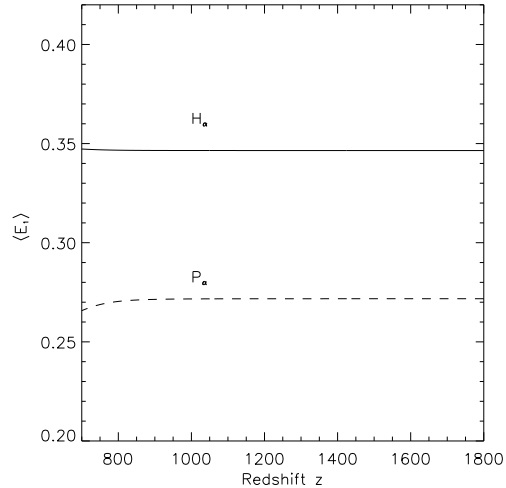


Figure 4. Polarisation coefficients E_1 associated to H_α (solid line) and P_α (dashed line) during recombination. Among all transitions listed in Table (1), only a few (one in case of H_α , 3 in case of P_α) contribute to the final value of E_1 .

3 COSMOLOGICAL HYDROGEN RECOMBINATION

The first scenario where resonant scattering may modify the pattern of the CMB polarisation anisotropies is precisely the cosmological hydrogen recombination. The CMB photons observed today were essentially last scattered during the redshift range $z \in [700, 1300]$, when the temperature of the Universe was sufficiently low to permit the formation of neutral atoms (Zeldovich, Kurt & Syunyaev 1968; Peebles 1968). During the process of recombination of the hydrogen and helium atoms, there was a net generation of photons which introduced distortions to the CMB blackbody spectrum. Except for the far Wien tail of the CMB, these distortions are expected to be very small (e.g. Rubiño-Martín et al. 2006), with typical values of the order of $\Delta I/I \approx 10^{-7}$, making their detection challenging. However, as studied in Rubiño-Martín et al. (2005), these lines leave also an imprint in the temperature angular power spectrum of the CMB. When observing the CMB at a frequency in the vicinity of a redshifted hydrogen line, the small optical depth of this transition influences the angular distribution of the CMB, due to the resonant scattering of the photons in this line. Therefore, we can use the optical depths connected with these transitions to explore the consequences of the overpopulation of the hydrogen atom levels at these epochs.

Here, we build upon the work of Rubiño-Martín et al. (2005) and compute the change in the CMB polarisation anisotropies during hydrogen recombination. In particular we focus on the main ($\Delta n = 1$) transitions of the Balmer and Paschen series, i.e. H_α and P_α : the first line provides the highest amplitude, whereas for the second line the corresponding redshifted frequency lies in the frequency band where most of the future CMB experiments will observe, and the foreground contamination is minimal. Note

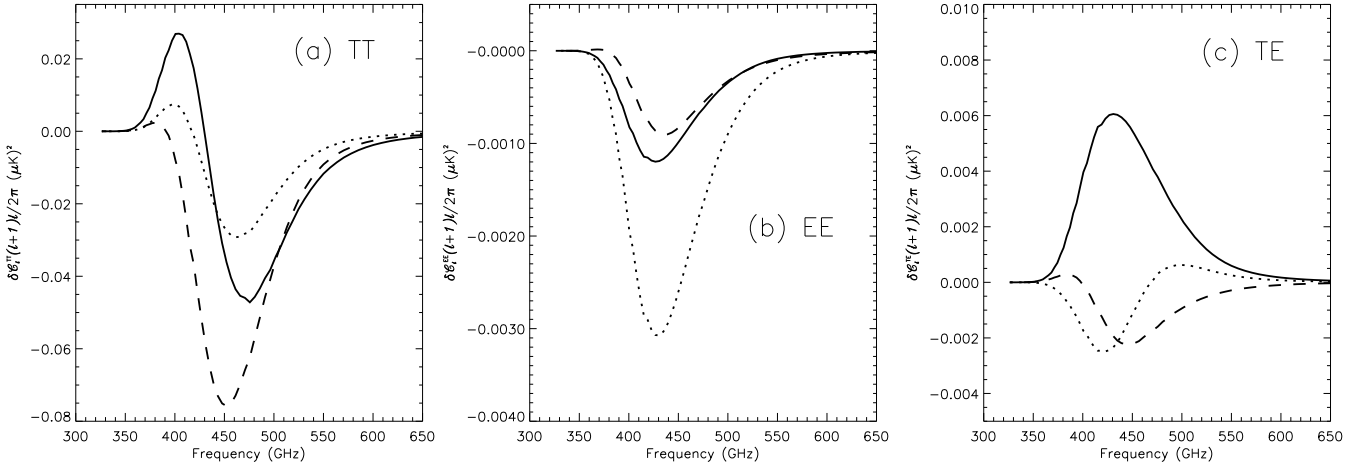


Figure 5. Change in the TT (a panel), EE (b panel) and TE (c panel) power spectra due to resonant scattering on H_α versus observing frequency. Solid, dashed and dotted lines correspond to multipoles $l = 783, 890$ and 1001 , respectively.

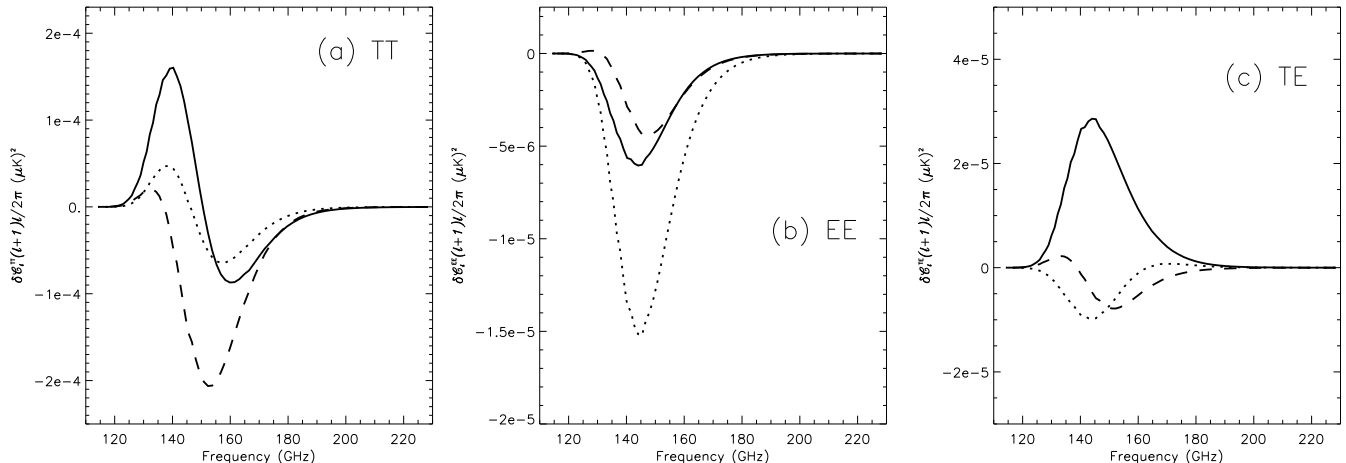


Figure 6. Same as in Figure (5), but for the P_α line. Note the different amplitude and frequency ranges.

that in addition to the bound-bound transitions described in Rubiño-Martín et al. (2005), there is also a contribution from the free-bound emission during recombination (Chluba & Sunyaev 2006). However, in the considered frequency band, their contribution to the total optical depth in the redshift range where recombination occurs is very small (Chluba et al. 2006).

For the H_α line, there are seven permitted (electric dipolar) transitions from the third shell ($n = 3$) to the second one ($n = 2$), depending on the particular configuration of the electronic orbital, intrinsic (spin) and total angular momenta of the levels involved. For the P_α case, the number of transitions amounts to seventeen. In Table 1 we list these transitions. For each line, the total optical depth observed at the corresponding frequency will be the sum of all contributing transitions. For each of transition $j \rightarrow i$, the optical depth τ_{ij} is given by (Sobolev 1946)

$$\tau_{ij} = \frac{A_{ji} \lambda_{ij}^3 [n_i(g_j/g_i) - n_j]}{8\pi H(z)}, \quad (27)$$

where A_{ji} is the spontaneous emission Einstein coefficient, λ_{ij} is the wavelength, and n_{i-j} , g_{i-j} are the populations and degeneracy factors of each of the two levels involved in the transition. $H(z)$ is the Hubble function at redshift z . In our computations, the populations for the different sublevels having different orbital angular momenta ($2s, 2p, 3s, 3p, 3d, 4s, 4p, 4d$ and $4f$) were tracked *independently*. Within each of these sublevels, we assumed that states having different total angular momenta j were *evenly* populated, i.e., as it is dictated by the Clebsch-Gordan coefficients and/or the statistical equilibrium condition. This is a reasonable assumption given that the energy differences between the different fine-structure sub-states of a given shell are four order of magnitude smaller than its energy. Given that the recombination lines are formed when the number of photons (per baryon) which are able to excite them falls below one (see e.g. Rubiño-Martín et al. (2006)), it is clear that the fine-structure sub-levels will maintain equilibrium due to the ambient CMB radiation field. Once we derive the

optical depth for each transition, we compute the average polarisation coefficient E_1 associated to both H_α and P_α as

$$E_1 = \frac{\sum_{ij} \tau_{ij} E_1^{ij}}{\sum_{ij} \tau_{ij}}, \quad (28)$$

with E_1^{ij} the polarisation coefficient for the particular transition $i \rightarrow j$. Figure (4) shows the behavior of both E_1 parameters through the recombination epoch in these circumstances: they show a somewhat constant value around ~ 0.35 for H_α and ~ 0.27 for P_α . This is mostly due to the presence of few dominant transitions (one for H_α , three for P_α) having the largest weight in eq.(28). In the case of H_α , it is the $P_{3/2} \rightarrow D_{5/2}$ transition driving the final value of E_1 ($\sim 60\%$ of the total τ), whereas for P_α these are $D_{7/2} \rightarrow F_{7/2}$ ($\sim 40\%$), $D_{3/2} \rightarrow F_{5/2}$ ($\sim 25\%$) and $D_{5/2} \rightarrow P_{3/2}$ ($\sim 7\%$).

Figure (5) displays the changes in the TT, EE and TE CMB angular power spectra versus observing frequency in the range where the H_α is redshifted. The (remarkably smaller) amplitudes for the P_α line are shown in figure (6). We have taken for the effective relative width of the line the value 5×10^{-3} , (σ_X/η_X , see eq.(26)). Solid, dashed and dotted lines correspond to multipoles $l = 783, 890$ and 1001 (corresponding for the maximum change in TE, TT and EE power spectra, respectively). These effects are considerably small, but however might be within the sensitivity limit of upcoming CMB experiments attempting to measure the B mode of polarisation anisotropies. Actually, when looking at H_α , the amplitudes for the change in the TT and TE power spectra are comparable with the expected amplitude of the B modes at intermediate angular scales ($l \in [60, 600]$) for a tensor to scalar ratio r of 0.03. Instead, the amplitudes for the changes in the EE power spectrum are closer to the same prediction for the B mode at larger angular scales, ($l \in [10, 30]$). Also, the definite l and frequency dependence of these changes in the power spectra should make their detection more tractable in practice, although at those frequencies dust is supposed to be dominating. In any case, we must conclude that, together with the characterisation of the B modes of CMB polarisation anisotropies, the detection of such small signals remains challenging for ongoing and upcoming observational efforts.

4 REIONISATION

In this Section, we revisit the imprint of resonant scattering of CMB photons off metals produced at the end of the dark ages and the beginning of reionisation. We shall attempt to build a somewhat realistic model for the production of heavy elements during cosmic times, and to obtain from it an amplitude for the effect of scattering on metals produced by the first stars.

4.1 Resonant Transitions

A search for resonant transitions falling in a frequency range that permits probing the resonant interaction with CMB photons in the redshift range $z \in [5, 50]$ yields the list shown

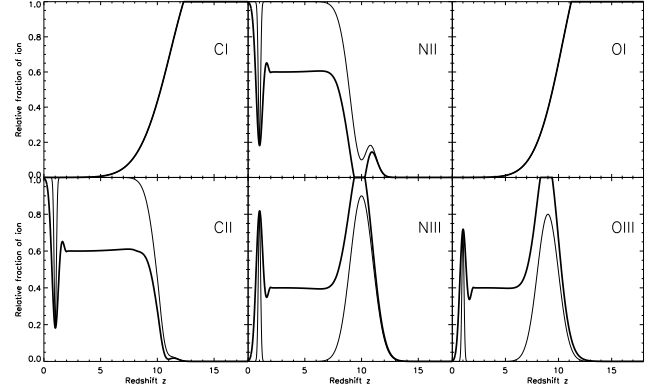


Figure 7. Relative fraction of ions for two different reionisation scenarios: in case (A) Pop III stars at $z \sim 10$ are able to ionise three times C, N and O only temporarily, so that those ions are absent until a new starburst at around $z \sim 1$ generates them again. This scenario is depicted by thin solid lines. In case (B), Pop III stars are able to keep a significant fraction of C, N and O ionised upto $z \sim 1$. In both cases, below $z \sim 1$, the star formation rate drops considerably, and so do the abundances of highly ionised atoms.

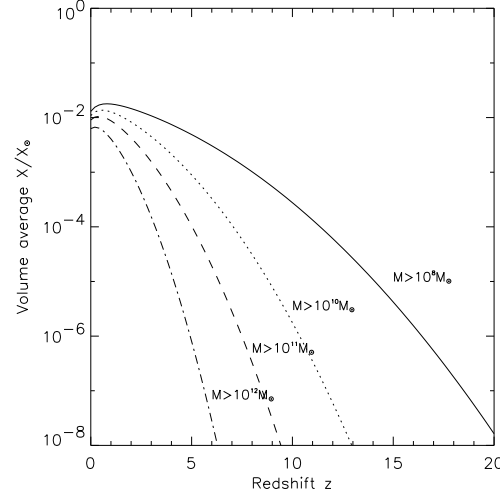


Figure 8. Volume average metallicity measured by a CMB experiment of angular resolution close to the arc-minute level and $\Delta\nu/\nu \sim 0.1$.

in Table 2. These are magnetic dipolar (M1) forbidden transitions, associated to elements and ions that should be more abundant during the epoch of cosmic dawn. After assuming a (volume-average) metal abundance of one part in one hundred compared to the solar value, we obtain typical values for the optical depth in the range $\tau_X \in [10^{-4}, 10^{-6}]$. I.e., we shall be working in the optically thin limit. Note that for the OI $63.2 \mu\text{m}$ line the polarisation coefficient is small ($E_1 = 0.01$), since it will have its repercussion in the forthcoming discussion.

Table 2. Resonant transitions in atoms/ions expected to be produced during Reionisation

Atom/Ion	λ (μm)	Oscillator strength f_i	Optical depth ($\nu = 250$ GHz, $X/X_\odot = 10^{-2}$)	Ionisation Potential (eV)	Excitation Potential (eV)	E_1
CI	609.7	1.3×10^{-9}	2.7×10^{-6}	11.3	0.0	1.00
CI	370.4	9.1×10^{-10}	2.7×10^{-6}	11.3	0.0	0.35
CII	157.7	1.7×10^{-9}	7.9×10^{-6}	24.4	11.3	0.50
NII	121.9	2.8×10^{-9}	4.5×10^{-6}	29.6	14.5	0.35
NII	205.2	3.9×10^{-9}	4.9×10^{-6}	29.6	14.5	1.00
NIII	57.3	4.7×10^{-9}	1.1×10^{-5}	47.5	29.6	0.50
OI	63.2	3.2×10^{-9}	4.3×10^{-5}	13.6	0.0	0.01
OI	145.5	1.9×10^{-9}	1.7×10^{-5}	13.6	0.0	0.00
OIII	51.8	6.5×10^{-9}	9.6×10^{-5}	54.9	35.1	0.35
OIII	88.4	9.3×10^{-9}	1.0×10^{-4}	54.9	35.1	1.00
OIV	25.8	1.0×10^{-8}	2.2×10^{-4}	77.4	54.9	0.50
SiI	68.5	4.9×10^{-9}	3.3×10^{-6}	8.1	0.0	0.35
SiI	129.7	6.2×10^{-9}	3.0×10^{-6}	8.1	0.0	1.00
SiII	34.8	7.9×10^{-9}	7.4×10^{-6}	16.4	8.1	0.50
SI	25.2	8.0×10^{-9}	4.1×10^{-6}	10.4	0.0	0.01
SI	56.3	4.8×10^{-9}	1.7×10^{-6}	10.4	0.0	0.00
SIII	18.7	1.8×10^{-8}	1.1×10^{-5}	34.8	23.3	0.35
SIII	33.8	2.4×10^{-8}	1.0×10^{-5}	34.8	23.3	1.00
SIV	10.5	2.6×10^{-8}	2.0×10^{-5}	47.2	34.8	0.50
FeI	24.0	1.7×10^{-8}	1.4×10^{-5}	7.9	0.0	0.04
FeI	34.7	2.1×10^{-8}	1.4×10^{-5}	7.9	0.0	0.03
FeI	54.3	1.6×10^{-8}	8.6×10^{-6}	7.9	0.0	0.01
FeII	26.0	1.7×10^{-8}	1.4×10^{-5}	16.2	7.9	0.05
FeII	51.3	1.9×10^{-8}	1.1×10^{-5}	16.2	7.9	0.02
FeII	87.4	1.1×10^{-8}	4.6×10^{-6}	16.2	7.9	0.00
FeIII	22.9	1.7×10^{-8}	1.4×10^{-5}	30.6	16.2	0.04
FeIII	105.4	7.8×10^{-9}	3.0×10^{-6}	30.6	16.2	0.00

4.2 A Toy Model for the Enrichment History of the Universe

In a similar way to BHMS, we shall consider two different models of reionisation: in case A we consider a reionisation scenario starting at $z \sim 12$, that is able to ionise twice a significant fraction of atoms like N, C and O *only temporarily* (down to redshift, say, $z \sim 7$). Only after a new starburst takes place in galaxies at $z \sim 1$ these ions appear again in the IGM. In case B, however, we observe the scenario where double ionised species are present in the IGM from $z \sim 10$ down to $z \sim 0.5$. The relative abundances of ions for C, N and O for this toy model are given in Figure (7): thin lines correspond to case A scenario, thick ones to case B. These elements correspond to the most abundance species that are able to interact with CMB photons in the frequency range of interest for us. Neutral Carbon and Hydrogen disappear as soon as first stars enter into scene for both reionisation models, but singly ionised species (CII, OII, NII) will eventually re-appear only if the flux of UV photons becomes lower than some threshold, (case A). The pattern of the polarisation anisotropies will be particularly sensitive to the presence or absence of certain species, as we next show.

In our toy model, we shall assume that metals are located in the interior of haloes more massive than a given threshold mass, here taken to be $M_{th} \sim 10^8 M_\odot$. Inside these haloes the metallicites are taken to reach the level of 5 times the solar metallicity. In practice, due to the finite

angular and spectral resolution of the CMB experiment, future observations will be sensitive to the *total* amount of atoms/ions within a given cosmological volume probed by the CMB experiment, i.e., they will be sensitive to the *volume average* metallicity of the IGM. In Figure (8) we show the volume average metallicity to be measured by an experiment whose PSF and frequency response probes a region comparable to the Hubble radius at each epoch, as it should be the case for experiments having a spectral resolution of $\Delta\nu/\nu \sim 0.1$. With this high dilution of the metallicities, the resulting amplitudes for the resonant scattering will be accordingly small. For simplicity, we shall restrict our analyses to the first ten lines considered in Table (2), since they correspond to the strongest line of the most abundant elements. The amplitudes and the overall behaviour of the IGM metallicity given in Figure (8) are not too different from observational estimates of Schaye et al. (2003); Aguirre et al. (2004); Ledoux et al. (2003) or Prochaska et al. (2003)

The fact that *all* existing lines will introduce some anisotropies at redshifts dictated by the observing and resonant frequencies translates into a non-trivial relation between observing frequency and *effective redshift of scattering*. In Figure (9a) we display this effective scattering redshift defined as

$$Z_{\text{eff}}(\nu) \equiv \frac{\sum_X z_X(\nu) \tau_X[z_X(\nu)]}{\sum_X \tau_X[z_X(\nu)]}, \quad (29)$$

where the sum is over the resonant lines under considera-

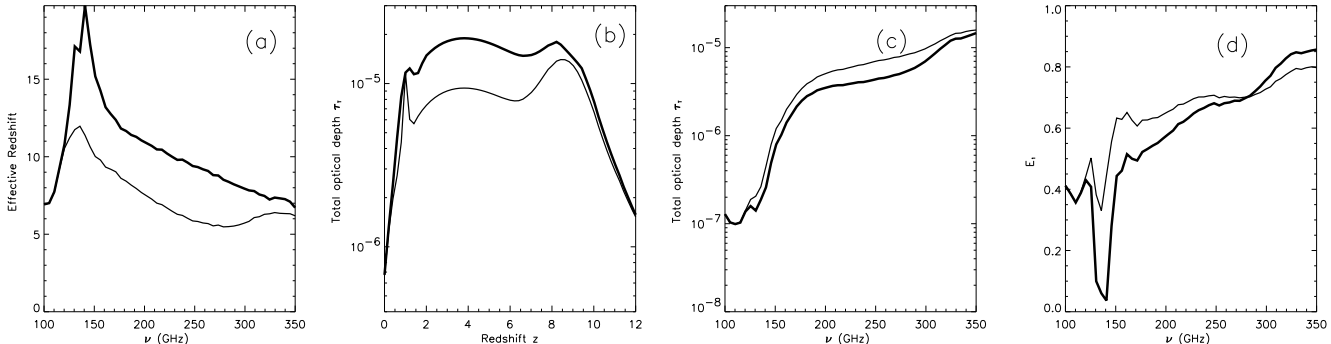


Figure 9. (a) Effective redshift versus observing frequency. (b) Total optical depth versus redshift (c) Total optical depth versus observing frequency. (d) Average polarisation coefficient versus observing frequency. In all panels, thin solid lines refer to case A reionisation scenario, thick solid lines to case B.

tion, and the optical depth for each transition is considered to be a function of the redshift corresponding to the observing frequency. Again, the thin solid line corresponds to case A, thick solid line to case B. Although there is a general trend to have smaller effective redshifts with increasing observing frequencies, the actual values may depend critically on the dominant lines at each frequency. This is the cause why panel (b) in Figure (9) (total optical depth τ_{Tot} versus redshift) differs so much from panel (c), (τ_{Tot} versus observing frequency): in panel (b) the distinction between the case A and case B scenarios looks much more feasible than in panel (c). As shown in panel (a), the case B scenario is observing, on average, at higher effective redshifts than case A, and this results in lower abundances and lower optical depths, making it more similar to the case A scenario. Both scenarios, case A and case B, could however be more easily distinguished if measurements of the effective polarisation coefficient were available; this coefficient, defined by

$$E_{1,\text{eff}}(\nu) \equiv \frac{\sum_X E_{1,X} \tau_X[\nu]}{\sum_X \tau_X[\nu]}, \quad (30)$$

is plotted in Figure (9d). The case B scenario (thick line) shows a profound dip at $\nu \sim 140$ GHz, and its origin is displayed in Figure (10). This last figure provides the relative weight of each transition to the total optical depth at a given observing frequency: dotted lines correspond to Carbon, dashed lines to Nitrogen and solid lines to Oxygen. Increasing thickness corresponds to increasing line of entry on Table 2 for a given element, from top to bottom. We see that neutral Carbon (thin dotted lines) dominate the total optical depth at low frequencies, i.e., high redshifts. On the contrary, at low redshifts (or high frequencies) the optical depth is dominated by ionised Oxygen (thick solid line). At intermediate redshifts, the lines from NII and CII compete (medium thickness dotted and dashed lines, respectively). The 63.2 μm OI line (thin solid line) becomes prominent at $\nu \sim 140$ GHz, and in case B scenario where there is little NII (since most of Nitrogen is in form of NIII) clearly dominates the total optical depth in a narrow redshift range. Since the polarisation coefficient associated to this transition is relatively low ($E_1 = 0.01$), it leaves a distinctive signature in the $E_{1,\text{eff}}$. Of course, these conclusions are consequences of our

particular choice of reionisation models, and are not generic.

Nevertheless, from a general point of view it is possible to state that the OI 63.2 μm transition will always leave the signature in the form of very low polarisation parameter $E_{1,\text{eff}}$, enabling its isolation from the rest of resonant lines. Further, it is a prediction for all models that the polarisation coefficient should increase with increasing frequency, since in this regime it would be dominated by the ionised species OIII, NII and CII. The measurement of polarisation anisotropies generated during reionisation via CMB scattering off metals would not only provide a consistency check for the detection in the temperature/intensity side, but would also shed more light on how reionisation took place. However, the detection of these polarisation anisotropies would require sensitivities of the order of 1–100 nK, and currently this is beyond the scope of most CMB polarisation projects.

5 DISCUSSION AND CONCLUSIONS

The measurement and interpretation of the polarisation *intrinsic* anisotropies of the CMB has remarkably tightened the constraints on several cosmological parameters, (Spergel et al. 2006). However, their characterisation is hampered by their low amplitude and the presence of contaminating signals. To date only anisotropies of the E mode of polarisation have been detected, but the detection of the B mode is currently the main goal of many ambitious CMB projects. The main difficulty that these projects will have to overcome is not only the extremely demanding level of sensitivity required to measure such a small signal, but also the exquisite control of systematics and foregrounds contaminants, the latter being usually orders of magnitude above the pursued component.

In this context, we have presented a study of the secondary anisotropies of the CMB polarisation field caused via resonant scattering in two different scenarios: the cosmological recombination and the cosmological reionisation. In both cases, the new polarisation anisotropies are E type, but of smaller amplitude than the intrinsic E type CMB polarisation fluctuations. In the recombination scenario, we have focused our analyses on the H_α line, giving rise

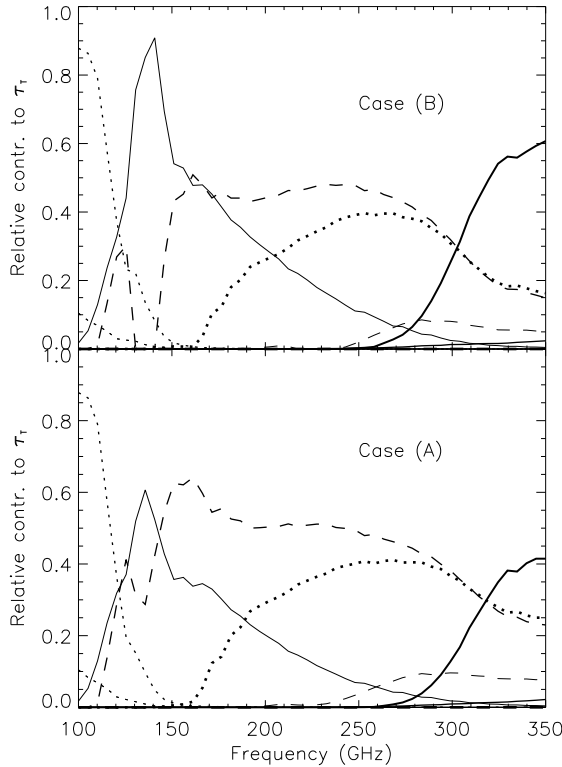


Figure 10. Relative contribution of each line to the total optical depth versus observing frequency. Dotted, dashed and solid lines correspond to Carbon, Nitrogen and Oxygen, respectively. Increasing line thickness corresponds to increasing line of entry in Table 2.

to the largest signal among all other transitions. We have found a definite and distinctive pattern in multipole and frequency space for the change of the TE and EE power spectra. This effect takes place in the frequency range $\nu \in [350, 600]$ GHz, and is maximum at multipoles $l \sim 900$. The amplitudes of these signals are in general comparable to those of the intrinsic B-mode polarisation anisotropies. In a scenario where CMB experiments have the sensitivity and systematics control level required to characterise the B-mode anisotropies, the access to the study of the fluctuations introduced by the H_α line should be then reachable.

The polarisation anisotropies introduced by resonant scattering off metals during reionisation would provide a concluding consistency check for the measurements carried out in the intensity/temperature side. At the same time, they would shed some light on *which* transitions are responsible for most of the measured effect. In particular, the OI 63.2 μm line tends to lower the average polarisation coefficient E_1 generated by all species, since it conserves very little memory of the polarisation of the scattered photon ($E_{1,63.2\mu\text{m}} = 0.01$). On the other hand, the dominant transitions associated to highly ionised species, like CIII and OIII, show relatively high values of E_1 , ($E_1 \in [0.5, 1]$). The requirements for detecting these signals are, however, even more demanding than in the recombination scenario: typical amplitudes are closer to the $n\text{K}$ level than to the μK

level, even below the amplitudes expected for the primordial B-mode polarisation anisotropies. The final detectability of this signal will be critically associated with the detectability of the primordial B-mode anisotropies: if the latter, at the end of the day, can be characterised with some given accuracy, then the possibility of pursuing signals that are still 5 to 50 times smaller could be formally addressed.

ACKNOWLEDGMENTS

CHM acknowledges fruitful conversations with R.Jimenez, Z.Haiman, J.García-Bellido and thanks L.Verde for carefully reading the manuscript. CHM is supported by NASA grants ADP04-0093 and NNG05GG01G, and by NSF grant PIRE-0507768. JARM acknowledges the hospitality of the Department of Physics and Astronomy of the University of Pennsylvania during his visit in June 2006.

REFERENCES

Aguirre, A., Schaye, J., Kim, T.-S., Theuns, T., Rauch, M., & Sargent, W. L. W. 2004, *ApJ*, 602, 38
 Barkats, D., et al. 2005, *ApJL*, 619, L127
 Basu, K., Hernández-Monteagudo, C., & Sunyaev, R. A. 2004, *A&A*, 416, 447, [BHMS]
 Chluba, J., & Sunyaev, R. A. 2006, *A&A*, 458, L29
 Chluba, J., Rubiño-Martin, J. A., & Sunyaev, R. A. 2006, ArXiv Astrophysics e-prints, arXiv:astro-ph/0608242
 Chandrasekhar, S. 1960, *Radiative Transfer* (New York: Dover)
 de Bernardis, P., et al. 1993, *A&A*, 269, 1
 Dickinson, C., et al. 2004, *MNRAS*, 353, 732
 Dubrovich, V. K. 1977, *Soviet Astronomy Letters*, 3, 128
 Dubrovich, V. K. 1993, *Astronomy Letters*, 19, 53
 Hamilton, D. R. 1947, *ApJ*, 106, 457
 Hernández-Monteagudo, C., & Sunyaev, R. A. 2005, *MNRAS*, 359, 597
 Hernández-Monteagudo, C., Verde, L., & Jimenez, R. 2006, *ApJ*, in press, ArXiv Astrophysics e-prints, arXiv:astro-ph/0604324
 Kuo, C. L., et al. 2004, *ApJ*, 600, 32
 Ledoux, C., Petitjean, P., & Srianand, R. 2003, *MNRAS*, 346, 209
 Loeb, A. 2001, *ApJL*, 555, L1
 Ma, C.-P., & Bertschinger, E. 1995, *ApJ*, 455, 7
 Page, L., et al. 2006, ArXiv Astrophysics e-prints, arXiv:astro-ph/0603450
 Peebles, P. J. E. 1968, *ApJ*, 153, 1
 Prochaska, J. X., Gawiser, E., Wolfe, A. M., Castro, S., & Djorgovski, S. G. 2003, *ApJL*, 595, L9
 Readhead, A. C. S., et al. 2004, *ApJ*, 609, 498
 Readhead, A. C. S., et al. 2004, *Science*, 306, 836
 Rubiño-Martín, J. A., Hernández-Monteagudo, C., & Sunyaev, R. A. 2005, *A&A*, 438, 461
 Rubiño-Martín, J. A., Chluba, J., & Sunyaev, R. A. 2006, *MNRAS*, 371, 1939
 Schaye, J., Aguirre, A., Kim, T.-S., Theuns, T., Rauch, M., & Sargent, W. L. W. 2003, *ApJ*, 596, 768
 Seljak, U., & Zaldarriaga, M. 1996, *ApJ*, 469, 437

Sobolev, V. V. 1946, Moving Atmospheres of Stars (Leningrad: Leningrad State Univ.; English transl. 1960, Cambridge: Harvard Univ. Press)

Spergel, D. N., et al. 2006, ArXiv Astrophysics e-prints, arXiv:astro-ph/0603449

Stancil, P. C., Loeb, A., Zaldarriaga, M., Dalgarno, A., & Lepp, S. 2002, ApJ, 580, 29

Sunyaev, R. A. & Zel'dovich, I. B. 1980, ARA&A, 18, 537

Switzer, E. R., & Hirata, C. M. 2005, PhRvD, 72, 083002

Zaldarriaga, M., & Harari, D. D. 1995, PhRvD, 52, 3276

Zaldarriaga, M., & Loeb, A. 2002, ApJ, 564, 52

Zaldarriaga, M., & Seljak, U. 1997, PhRvD, 55, 1830

Zeldovich Y. B., Kurt V. G., Syunyaev R. A., 1968, ZhETF, 55, 278

APPENDIX A: THE DRAG FORCE

A net flow of CMB photons will exert some drag force on a fluid of atoms that are able to interact with the photon gas via some resonant transition X , with drag force defined as "rate of momentum exchange per unit time and unit volumen". Here we detail the calculation of the drag force exerted on the atom fluid for a given frequency of the CMB field. The expression will be integrated in atom momentum and photon frequency to yield the well-known result that the drag force will be proportional to $f_0(\nu_X, \eta)\Psi_1\nu_X^3n_X(\eta)$, with $n_X(\eta)$ the average comoving number density of atoms taking part in the resonance.

For a given transition X , the optical depth for scattering at a given frequency is given by

$$\sigma(\nu) = \frac{c^2}{8\pi\nu_X^2} \frac{g_u}{g_l} A_X \Phi(\nu) \frac{1 - \exp(-\frac{h\nu_X}{kT_{ex}})}{1 + \frac{g_u}{g_l} \exp(-\frac{h\nu_X}{kT_{ex}})} \quad (A1)$$

where A_X is the Einstein coefficient for spontaneous emission of the transition, g_u and g_l the statistical weights for the upper and lower levels of the transition, respectively, and T_{ex} represents the excitation temperature, which in case of equilibrium with the radiation field would correspond to the CMB temperature. Finally, $\Phi(\nu)$ represents the line profile.

The photon flow and drag force are taken to be parallel to the polar axis in the integration on \mathbf{q} , (i.e., $\hat{\mathbf{n}}$). Only the dipole term $f_0(q, \eta)\Psi_1(\mathbf{k}, q, \eta)$ will contribute in the momentum integration, and hence the drag force amplitude, expressed in terms of unit volumen occupied by the atom fluid, can be written as

$$F_\gamma^X = (-4\pi i) \int dq q^2 f_0(q, \eta) \Psi_1(\mathbf{k}, q, \eta) q c \sigma_X \int_\Sigma d\mathbf{p} f_X(\mathbf{p}, \eta). \quad (A2)$$

For simplicity, we have introduced a frequency-independent cross-section σ_X , which in practice is equivalent to approximate the profile function by a top-hat function of a certain width $\Delta\nu$. Thus, the expression for σ_X is given by $\sigma(\nu)/(\Delta\nu\Phi(\nu))$. Note that $f_0\Psi_1 \equiv \sum_{j=1}^2 f_0^j \Psi_1^j$ corresponds to the sum over polarisation states of the first momentum of the photon distribution function expansion introduced in eq.(3). The atom fluid is assumed to be described by a Maxwell-Boltzmann distribution function (f_X) in thermal equilibrium with the CMB photon field:

$$f_X(\mathbf{p}, \eta) = \frac{n_X(\eta)}{[2\pi m_X k_B T]^{3/2}} \exp\left(-p^2/[2\pi m_X k_B T]\right), \quad (A3)$$

with $T = T_0(1 + z[\eta])$ the CMB temperature monopole. The dominium of integration Σ is defined by the subset of possible values of p and μ ($d\mathbf{p} = p^2 dp d\mu d\phi$) verifying the resonance condition

$$\mathbf{p} \cdot \hat{\mathbf{n}} = m_X c \left(1 - \frac{\nu_X}{\nu}\right), \quad (A4)$$

that is,

$$\mathbf{p} \cdot \hat{\mathbf{n}} \in \left[\min\left(m_X c \left(1 - \frac{\nu_X}{\nu} \pm \frac{A_X}{4\pi}\right)\right), \max\left(m_X c \left(1 - \frac{\nu_X}{\nu} \pm \frac{A_X}{4\pi}\right)\right) \right], \quad (A5)$$

with $A_X/2\pi$ the intrinsic natural width of the line. Since the integrand does not explicitly depend on μ , we can integrate on this variable, replacing $d\mu$ by $\Delta\mu = m_X c A_X/(2\pi\nu p)$. Note that $\Delta\mu \leq 2$, and so

$$p \geq \frac{m_X c}{2} \frac{A_X}{2\pi\nu}. \quad (A6)$$

Note, as well, that from the resonance condition of eq.(A4) we must have

$$p \geq m_X c \left(1 - \frac{\nu_X}{\nu}\right), \quad (\nu > \nu_X), \quad (A7)$$

$$p \geq m_X c \left(\frac{\nu_X}{\nu} - 1\right), \quad (\nu < \nu_X). \quad (A8)$$

Therefore, the minimum value of p allowed in the integration is

$$p_{\min}(\nu) = \max\left[\frac{m_X c}{2} \frac{A_X}{2\pi\nu}, \pm m_X c \left(1 - \frac{\nu_X}{\nu}\right)\right]. \quad (A9)$$

The first value will be used only if $|\nu_X/\nu - 1| \leq A_X/(4\pi\nu_X)$, and will give a negligible contribution, as we shall see. The maximum value for p will be $p_{\max} = m_X c$. However, it will be approximated by infinity in the integral, since $m_X c \gg \sqrt{2m_X k_B T}$ in our case. After introducing $\Delta\mu$ in eq.(A2), trivially integrating in $d\phi$, and integrating in p one obtains

$$F_\gamma^X = (-4\pi i) \int dq q^2 f_0 \Psi_1 q c \sigma_X n_X \frac{A_X}{2\pi\nu} \frac{m_X c}{\sqrt{2m_X k_B T}} \exp\left(-p_{\min}^2(\nu)/(2m k_B T)\right). \quad (A10)$$

This equation shows that, for a given frequency, the fraction of atoms being affected by the drag of CMB photons is

$$r_X = \frac{A_X}{2\pi\nu} \frac{m_X c}{\sqrt{2m_X k_B T}} \exp\left(-p_{\min}^2(\nu)/(2m k_B T)\right). \quad (A11)$$

From eq.(A9), it is clear that the largest contribution of the integral in eq.(A10) comes from the vicinity of $q = q_X = h\nu_X/c$, and this allows rewriting most of the terms out of the q integral, yielding

$$F_\gamma^X \simeq (-4\pi i) q_X^2 (f_0 \Psi_1)_{q_X} q_X (c \sigma_X n_X) \frac{A_X}{2\pi\nu_X} \frac{m_X c}{\sqrt{2m_X k_B T}}$$

$$\int_{\text{line}} dq \exp\left(-p_{\min}^2(\nu)/(2m k_B T)\right) \quad (A12)$$

We next sweep the vicinity of the line, and split this integral in three separate ones, according to the three different possible values of $p_{\min}(\nu)$. The final result is:

$$F_{\gamma}^X \simeq (-4\pi i)(c \sigma_X n_X) \frac{hA_X}{2\pi c} q_X^2 (f_0 \Psi_1)_{q_X} q_X \left[\operatorname{erfc} \left(\frac{A_X}{4\pi\nu_X} \right) + \frac{mc}{\sqrt{2\pi m_X k_B T}} \frac{A_X}{2\pi\nu_X} \exp - \left(\frac{m_X c}{\sqrt{2m_X k_B T}} \frac{A_X}{4\pi\nu_X} \right)^2 \right]. \quad (\text{A13})$$

The first term in brackets accounts for the integral throughout the thermal width of the line. The argument of the complementary error function is very close to zero, so this term is very close to unity. That is, practically *all* atoms are experiencing some drag force exerted by the CMB photons. The second term in brackets provides the integral within the natural width of the line, and its contribution can be safely neglected. Hence

$$F_{\gamma}^X \simeq (-4\pi i)(c \sigma_X n_X) \frac{hA_X}{2\pi c} q_X^2 (f_0 \Psi_1)_{q_X} q_X. \quad (\text{A14})$$

I.e., the momentum $q_X = h\nu_X/c$ is transferred to *all* atoms at a rate given by $c \sigma_X n_X$ in a momentum shell of radius q_X and thickness $hA_X/(2\pi c)$.